Appl Biochem Biotechnol (2014) 174:984–997
DOI 10.1007/s12010-014-0984-1

Biofunctionalized Gold Nanoparticle-Conducting Polymer Nanocomposite Based Bioelectrode for CRP Detection

Sujeet K. Mishra · Vikash Sharma · Devendra Kumar · Rajesh

Received: 13 January 2014 / Accepted: 19 May 2014 /
Published online: 4 June 2014

Abstract An electrochemical impedance immunosensing method for the detection and quantification of C-reactive protein (αCRP) in phosphate buffered saline (PBS) is demonstrated. The protein antibody, Ab-αCRP, has been covalently immobilized on a platform comprising of electrochemically deposited 3-mercaptopropionic acid-capped gold nanoparticles Au(MPA)-polypyrrole (PPy) nanocomposite film of controlled thickness onto an indium tin oxide-coated glass plate. The free carboxyl groups present on the nanocomposite film have been used to site-specifically immobilize the Ab-αCRP biomolecules through a stable acyl amino ester intermediate generated by *N*-(3-dimethylaminopropyl)-*N*′-ethyl carbodiimide hydrochloride and *N*-hydroxysuccinimide. The nanocomposite film was characterized by atomic force microscopy, high-resolution transmission electron microscopy, Fourier transform infrared spectroscopy, and electrochemical techniques. The bioelectrode was electrochemically analyzed using modified Randles circuit in terms of constant phase element (CPE), electron transfer resistance (R_{et}), and Warburg impedance (Z_w). The value of n, a CPE exponent used as a gauge of heterogeneity, for the Au-PPy nanocomposite film was found to be 0.56 which is indicative of a rather rough morphology and porous structure. A linear relationship between the increased ΔR_{et} values and the logarithmic value of protein antigen, Ag-αCRP, concentrations was found in the range of 10 ng to 10 μg mL^{-1} with a R_{et} sensitivity of 46.27 Ω cm^2/decade of [Ag-αCRP] in PBS (pH 7.4).

Keywords Electrochemical impedance spectroscopy · Conducting polymer · Gold nanoparticles · Protein immobilization

Introduction

Electrically conducting materials based on π-π-conjugated polymers such as polythiophene, polypyrrole (PPy), and polyaniline have been intensively studied because of their remarkable

S. K. Mishra · V. Sharma · Rajesh (✉)
CSIR-National Physical Laboratory, Dr. K.S. Krishnan Road, New Delhi 110012, India
e-mail: rajesh_csir@yahoo.com

S. K. Mishra · D. Kumar
Department of Applied Chemistry, Delhi Technological University, Bawana Road, Delhi 110042, India

mechanical and electrical properties, which can be exploited in actuators, sensors, and electrochromic devices [1–3]. Polymeric nanocomposite material based on hybrid materials comprising of polymer, nanomaterials, and more components has aroused a wide academic and technological interest in recent years. PPy, one of the most widely studied organic conducting polymers, has been widely used for sensing application due to its advantages of permitting a facile electronic charge flow through the polymer matrix, easy preparation, high conductivity, and good stability [4, 5]. The resonance-stabilized π-conjugated system structure of PPy allows the incorporation of ions, nanoparticles, nanowires of metals, or metal oxides which can significantly improve or tune the electrical and mechanical properties of nanocomposites [6, 7]. The incorporation of functionalized nanomaterial in the polymer matrix can act as an efficient template for the immobilization of biomolecules and, thus, help in overcoming the denaturation of the biomolecules which occur if they are directly adsorbed or entrapped inside the polymer matrix. Gold nanoparticles (Au NPs) with their unique size-dependent properties such as large specific interface area, desirable biocompatibility, and high surface free energy of nanosized particles have been widely used for the fabrication of biosensor with enhanced analytical performance as the immobilization interface [8–10]. The Au NPs incorporated into a polymer substrate is known to provide a physiological environment similar to that of biomolecules in their native system. In addition, good electrical property of the intercalated Au NPs will improve the conductivity of the resultant film and enhance the current response of the sensors [11].

C-reactive protein (αCRP) is a homo-pentameric protein belonging to the pentraxin family having two chain structures and also can conform the circular to five of the same size of homologous subunits [12]. Each subunit is linked to two calcium ions through an electrostatic salt bridge [13] and one subunit is composed of 224 amino acids having a molecular mass about 25 kDa. CRP is an acute phase protein produced by hepatocytes in response to circulating IL-6, IL-1, and TNFα. It plays an important role in host defense as a pro-inflammatory mediator and activator of the complement pathway. CRP has traditionally been used as a reliable marker for tissue injury, infection, and inflammation. However, studies have shown that CRP is also implicated in the development of cardiovascular diseases, such as atherosclerosis, angina, coronary heart disease, peripheral artery disease, myocardial infarction, and stroke [14]. The risks for cardiovascular diseases defined by the American Heart Association and the Center for Disease Control and Prevention are low for a CRP concentration below 1.0 mg/L, moderate for a CRP level from 1.0 to 3.0 mg/L, and high for concentrations over 3.0 mg/L [15]. The methods usually adapted for the determination of CRP include immunonephelometry, radial immunodiffusion, immunoturbidimetry, and immunochemiluminescence and enzyme immunoassay like ELISA. However, the disadvantages of these tests are the long reaction times (several hours) of the multiple steps involved and the requirement of trained personnel and expensive reagents. Over the last few years, the focus has been shifted to more powerful, noninvasive, and informative electrochemical impedance spectroscopy (EIS)-based immunosensing methods for detection of the protein biomarkers [16–18]. Unlike voltammetric techniques, EIS is nondestructive to the biological interactions because it works under very small amplitude perturbation from steady state. As one of the electrochemical technologies, EIS is rapidly used for the investigation of interfacial electrical properties of any kind of solid or liquid material which is connected to, or part of, an appropriate electrochemical transducer and is one of the major analytical tools used in clinical diagnostics, food safety and quality control, biological analysis, and environmental monitoring [19–22]. The EIS method is simple, sensitive, cost-efficient, and is particularly well-suited for the characterization and detection of binding events on

the transducer surface based on capacitive changes or changes in charge transfer resistance.

In this paper, 3-mercaptopropionic acid-functionalized gold nanoparticles, Au(MPA), were electrochemically intercalated in the PPy matrix using a one-step electrochemical method to produce a Au(MPA)-PPy nanocomposite film of controlled thickness on indium tin oxide (ITO)-coated glass plate. The nanocomposite film-modified electrode contains free pendant carboxylic groups which are used for site-specific covalent binding of protein antibody (Ab-αCRP) via carbodiimide coupling. The incorporation of Au(MPA) not only improves the electrochemical stability of the nanocomposite film but the nanoparticles also act as versatile and efficient templates for the immobilization of biomolecules. The site-specific attachment of the biomolecules to Au(MPA) having very large surface area and good biocompatibility helps in retaining the biological activity of electrode-bound proteins, improves orientation of immobilized antibodies, and increases protein loading. The composition, morphology, and microstructure of the as-obtained Au(MPA)-PPy nanocomposite film and that of the bioelectrode were characterized by spectroscopic and electrochemical techniques. The performance of the bioelectrode was analyzed by means of EIS using the increase in charge transfer resistance (R_{et}) upon binding of complementary protein antigen, Ag-αCRP, as an index of sensor response.

Materials and Methods

Reagents

Ab-αCRP (Cat 4C28 mAbC2) and Ag-αCRP (Cat 8C72) were obtained from Hytest (Turku, Finland). Mouse immunoglobulin-G (Ag-IgG) (Cat IGP3) was obtained from GENEI, Bangalore. Tetra-chloroauric (III) acid ($HAuCl_4$) was obtained from Himedia Pvt. Ltd. India. Tri-sodium citrate ($Na_3C_6H_5O_7$), pyrrole, *p*-toluene sulfonic acid (pTSA), 3-mercaptopropionic acid 99 % (MPA), *N*-(3-dimethylaminopropyl)-*N*′-ethyl carbodiimide hydrochloride (EDC), and *N*-hydroxysuccinimide 98 % (NHS) were obtained from Sigma-Aldrich. All other chemicals were of analytical grade and used without further purification.

Apparatus

Electro polymerization, cyclic voltammetry (CV), and electrochemical impedance spectra (EIS) measurements were done on a PGSTAT302N, AUTOLAB instrument from Eco Chemie, The Netherlands. All measurements were carried out in a conventional three-electrode cell configuration consisting of a modified ITO-glass electrode as working electrode, Ag/AgCl reference electrode, and a platinum counter electrode. The EIS experimental data were circuit-fitted by GPES (General purpose electrochemical system version 4.9, Eco Chemie) software and the values of EIS parameters were obtained. High-resolution transmission electron microscopy (HRTEM) experiments were performed using a HRTEM model (Tecnai G2 F30 STWIN) operated at an electron accelerating voltage of 300 kV using electron source as field emission gun. Atomic force microscope (AFM) images were obtained in a noncontact mode on a Nanoscope 5, VEECO Instrument Ltd., USA. XRD patterns were recorded using Bruker AXS Advance D8 powder X-ray diffractometer. A Fourier transform infrared (FTIR) spectrum was taken on a FTIR spectrometer, Nicolet 5700.

Preparation of Ab-αCRP/Au(MPA)-PPy/ITO-Glass Bioelectrode

Au(MPA) nanoparticles were prepared using the method as reported earlier [23]. Briefly, 50 μL of 5 mM aqueous solution of MPA was added to 5 mL of Au colloidal solution under constant stirring for 30 min till the color changes from wine red to blue. The change in color signifies the formation of a stable thiol monolayer of MPA on Au NPs. The Au(MPA)-PPy nanocomposite film was electrochemically deposited on ITO-glass plates (0.25 cm^2) (10 Ω/□) using the chronopotentiometric method by imparting a fixed current density of 1 mA cm^{-2} to an aqueous solution (1.5 mL) of 50 mM Au(MPA), 25 mM pyrrole, and 25 mM pTSA with a total injected charge density of 250 mC cm^{-2}. The pendant carboxyl groups of the Au(MPA)-PPy nanocomposite film-modified electrode were then activated by immersing in an aqueous solution containing 30 mM NHS and 150 mM EDC for 1 h followed by washing with distilled water and dried under N_2 gas flow. The protein antibody, Ab-αCRP, was then site-specifically immobilized on NHS/EDC-treated Au(MPA)-PPy electrode by incubating it in PBS (pH 7.4) containing 100 μg mL^{-1} of Ab-αCRP, for an overnight period at 4 °C, followed by washing with PBS and drying with N_2. The superficial nonspecific binding sites and the unbound free carboxyl groups of Ab-αCRP/Au(MPA)-PPy/ITO-glass bioelectrode were blocked by incubating the bioelectrode in 1 % bovine serum albumin (BSA) (*w*/*v*), followed by washing with distilled water, dried under N_2 flow, and then are stored at 4 °C.

Results and Discussion

Microstructural Characterization

Figure 1 shows the XRD pattern of both pristine PPy film and that of the Au-PPy nanocomposite film. The appearance of two additional peaks in the XRD pattern of the nanocomposite film in comparison to pristine PPy at 2θ=36.8° and 44.5° corresponding to (111) and (200) planes of Au indicates the presence of Au NPs in the nanocomposite film. The low intensity of these peaks is due to the complete enclosure of the Au NPs by PPy film. The average crystallite size (D) of Au(MPA) nanoparticles was estimated by using Scherrer's equation (Eq. 1):

$$D = 0.89\lambda \Big/ \beta\cos\theta \tag{1}$$

where λ is the wavelength of X-ray (0.1541 nm), β is the width at half maximum of diffraction peak (FWHM), and θ is the diffraction angle. The average value of D was found to be ~6 nm.

HRTEM images (Fig. 2) of the Au(MPA)-PPy nanocomposite film on a Cu grid depict a homogeneous overlap of Au(MPA)-NPs and PPy in the nanocomposite matrix without any perforation at the interface between these two types of species in the composite. The microstructural elucidation of the composite illustrates Au(MPA)-NPs with an average size of about 6 nm. Selected area electron diffraction pattern (SAEDP) of Au(MPA)-NPs shows a diffuse Debye ring overlapped on spotty pattern of Au-face centered cubic (fcc) structure with two prominent planes of hkl: 111 and 200. Although PPy showed a featureless contrast of amorphous structure, in some regions, it depicted an ultrafine crystallinity at atomic scale with an interplanar spacing of 0.18 nm.

The electrode configuration was further investigated with pristine PPy, Au(MPA)NPs-PPy, and Ab-αCRP/Au(MPA)-PPy films using FTIR spectroscopy (Fig. 3). The peaks obtained at 1,508 and 1,407 cm^{-1} correspond to pyrrole ring fundamental vibration, while the peak at

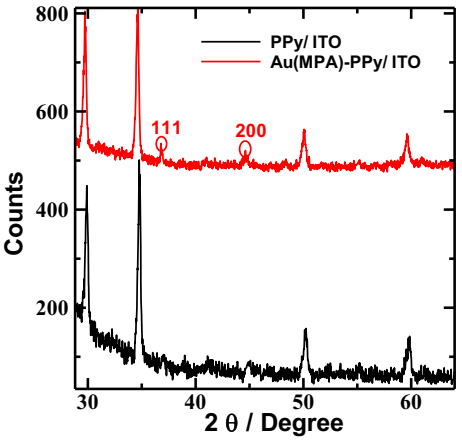

Fig. 1 XRD pattern of pristine PPy and Au(MPA)-PPy composite

3,590 cm^{-1} is attributed to N-H stretch vibration. The peaks at 1,176 and 1,040 cm^{-1} could be assigned to=C-H in-plane vibration. The principal peak obtained at 1,704 cm^{-1} for Au(MPA)-PPy composite film is ascribed to the C=O absorption vibration of carboxylic groups which further establishes the presence of carboxyl (MPA) groups in the Au(MPA)-PPy nanocomposite film. After the immobilization of the protein antibody, Ab-αCRP, the peak at 1,704 cm^{-1} gets shifted to 1,613 cm^{-1} (NH bending) indicating the formation of amide bond with antibody molecules. Moreover, the additional band seen at around 3,342 cm^{-1} represents N-H stretching of the amide.

The surface morphology was further investigated by taking the subtle AFM surface topographical images of the Au(MPA)NPs-PPy composite film and biofunctionalized Ab-αCRP/Au(MPA)NPs-PPy film-based electrode, as shown in Fig. 4. The surface roughness

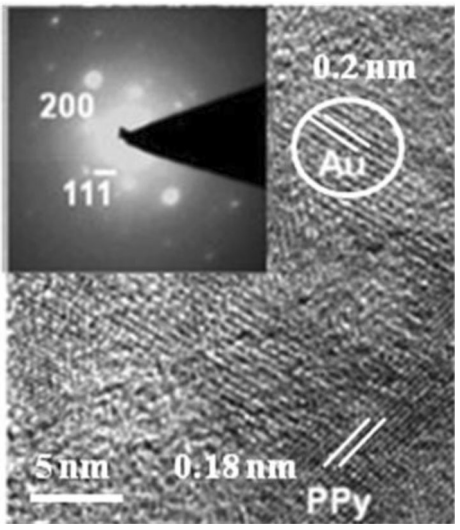

Fig. 2 HRTEM images of Au(MPA)-PPy composite atomic scale image of Au and PPy. *Inset*: composite SAEDP from crystalline Au and amorphous PPy

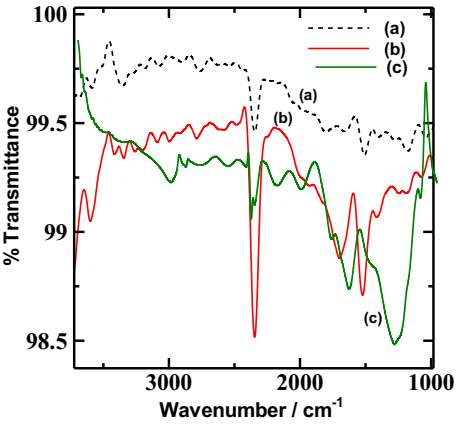

Fig. 3 FTIR spectra of *a* PPy, *b* Au(MPA)NPs-PPy, and *c* Ab-αCRP/Au(MPA)-PPy

parameter (R_a) is used to characterize the topography in terms of irregularity and height distribution. Figure 4(a) shows asymmetric grainy structure of the Au(MPA)-PPy composite film-based electrode with the formation of some large grains (30–40 nm) due to agglomeration of nanometric subunits (10–15 nm) at certain places. The corresponding R_a value so obtained for the composite film is 1.77 nm. The surface morphology of the nanocomposite film changes from a grainy structure to a comparatively bigger and globular feature with a R_a value of 2.17 nm after the immobilization of protein Ab-αCRP (Fig. 4(b)). This may be due to the noncompact assembly of the protein molecules over the composite film resulting from the covalent bonding of protein to free carboxyl groups of Au(MPA)NPs over the PPy matrix.

Electrochemical Characterization of Bioelectrode

EIS, a powerful diagnostic tool for the investigation of the electrical behavior of an electrochemical system, has been used to provide information on the impedance changes of the bioelectrode in the modification process. In EIS, a low-amplitude (50 mV peak-to-peak) sinusoidal potential is superimposed on a fixed DC potential that promotes the redox reaction of the probe. The sinusoidal current obtained is then used to calculate the impedance over a wide frequency range. A Nyquist plot (imaginary impedance ($-Z''$) versus real impedance (Z')) often reveals different features depending on the nature of the electrode reaction. The experimental impedance spectra may be interpreted either with reference to detailed physical models, or through equivalent circuits, representing the different processes involved in the description of the system with discrete electric elements. We have used in the present work the modified Randles equivalent circuit (inset of Fig. 5a) to take into account the finite spatial extension of the system under study. Randles equivalent circuit includes the following four elements: (i) the ohmic resistance of the electrolyte solution, R_s; (ii) the Warburg impedance, Z_w, resulting from the diffusion of ions from the bulk electrolyte to the electrode interface; (iii) electron transfer resistance, R_{et}, which exists if a redox probe is present in the electrolyte solution; and (iv) the interfacial double layer capacitance (C_{dl}) between an electrode and a solution; a constant phase element (CPE) is used in place of C_{dl} to explain the inhomogeneity, roughness or fractal geometry, and porosity of the electrode surface [24]. The impedance of CPE can be expressed by Eq. 2:

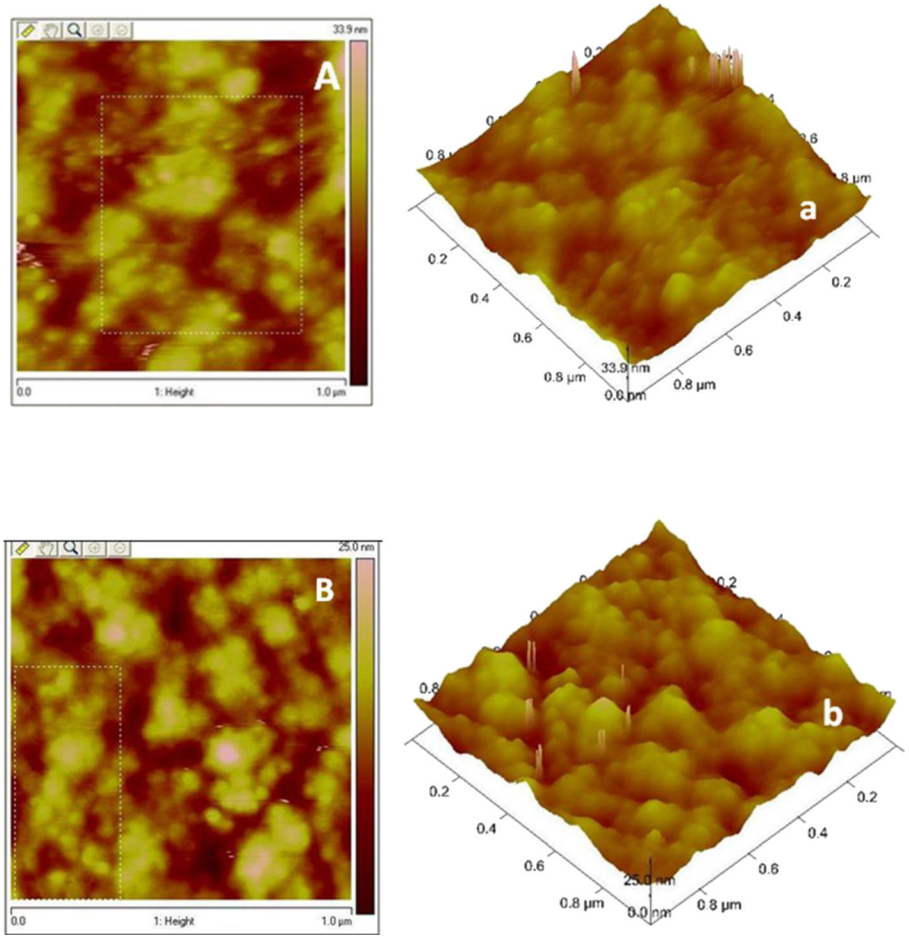

Fig. 4 2D (*A*) and 3D (*a*) AFM images of Au(MPA)-PPy/ITO-glass; 2D (*B*) and 3D (*b*) AFM images of Ab-αCRP/Au(MPA)-PPy/ITO-glass bioelectrode

$$Z_{\mathrm{CPE}}(\omega) = 1 \Big/ Y_0 (j\omega)^n \tag{2}$$

where Y_0 is a constant, j is the imaginary number, ω is the angular frequency, and n is the CPE exponent which can be used as a gauge of the heterogeneity and gives details about the degree of surface inhomogeneity (roughness). Depending on the value of n, CPE can represent resistance (n=0), capacitance (n=1, Y_0=C), inductance (n=−1), or Warburg element (n=0.5).

The EIS measurement was conducted in PBS (pH 7.4, 0.1 M KCl) solution containing 2 mM $[Fe(CN)_6]^{3-}$/$[Fe(CN)_6]^{4-}$, in the frequency range from 0.1 to 100 kHz at an AC voltage of 0.50 V. The Nyquist plots obtained after different steps of modification of the ITO-glass electrode are illustrated in Fig. 5a and the corresponding R_{et} values are listed in Table 1. The fitting accuracy of the modeled Randle's equivalent circuit parameters to the observed experimental values is validated by the very small chi-squared function (χ^2) value (~10^{-4}). A lower R_{et} value of 25.50 Ω cm^2 with a higher Y_0 value of 89.9 μF cm^{-2} (Table 1) obtained

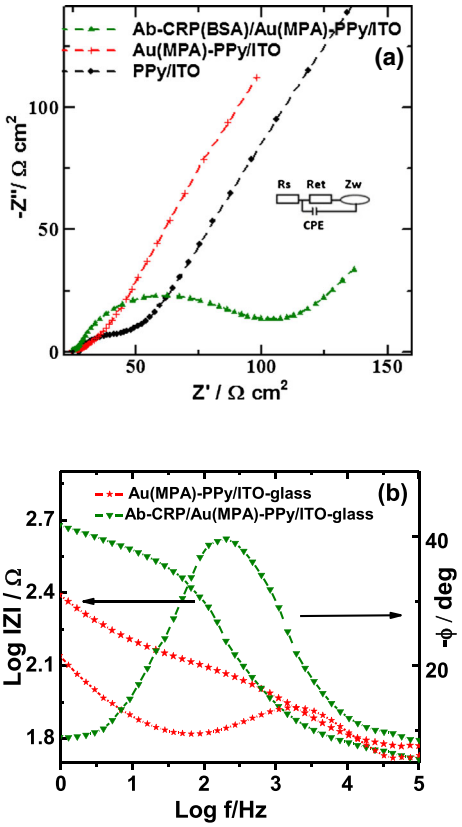

Fig. 5 **a** Nyquist plots obtained for pristine PPy/ITO-glass, Au(MPA)-PPy/ITO-glass, and Ab-αCRP/Au(MPA)-PPy/ITO-glass in PBS (pH 7.4,0.1 M KCl) containing 2 mM $[Fe(CN)_6]^{3-/4-}$ and **b** corresponding Bode plots of Au(MPA)-PPy/ITO-glass and Ab-αCRP/Au(MPA)-PPy/ITO-glass

for Au(MPA)-PPy/ITO-glass electrode in comparison to PPy/ITO-glass electrode (R_{et}= 45.50 Ω cm^2 and Y_0=69.8 μF cm^{-2}) suggests a faster electron transfer via the Au-PPy nanocomposite film toward the electrode surface. The presence of Au nanoparticles which act as tiny conduction centers enables facilitating direct and fast electron transfer between the redox probe species present at the electrode/solution interface and the transducer. The surface inhomogeneity is another factor which affects the permeability of ions responsible for the fast electrode interfacial electron transport. The small value of n (=0.56) shown in Table 1 for Au(MPA)-PPy/ITO-glass electrode is indicative of a rather rough morphology and porous structure and is probably also associated with electron hopping along the polymer backbone leading to a fast electron transfer through the transducer. After the covalent immobilization of protein, Ab-αCRP on Au(MPA)-PPy/ITO-glass electrode surface, the R_{et} value increased to 88.25 Ω cm^2, while the corresponding Y_0 value decreases to 43.2 μF cm^{-2}. This increment in the R_{et} value is due to the insulating behavior of the immobilized protein antibody layer on the bioelectrode surface, which acts as an electron communication and mass transfer blocking layer, thereby hindering the access of the redox probe toward the electrode surface and thus resulting in a sluggish electron transfer kinetic.

Although the Nyquist plots are more commonly displayed, the data in a Nyquist plot is often poorly resolved (particularly at high frequencies), and the explicit frequency dependence

Table 1 EIS characteristic parameters at various stages of surface modification of the electrodes

Electrodes	ΔE (mV)	R_{et} (Ω cm^2)	CPE		k^0 (m s^{-1})	Z_w (Ω cm^2)	δ (μm)
			Y_0 (μF cm^{-2})	n			
PPy/ITO-glass	128	45.50	69.8	0.748	1.16×10^{-3}	5.10×10^{-3}	56.7
Au(MPA)-PPy/ITO	96.1	25.50	89.9	0.593	2.08×10^{-3}	3.01×10^{-3}	49.2
Ab-αCRP/Au (MPA)-PPy/ITO	133.5	88.25	43.2	0.789	0.47×10^{-3}	2.01×10^{-3}	58.0

ΔE redox peak potential, R_{et} charge transfer resistance, *CPE* constant phase element, k^0 apparent rate constant, Z_w Warburg resistance, δ diffusion layer thickness

is not displayed. Hence, the Bode plot has been used to provide a clearer description of the electrochemical system's frequency-dependent behavior. The Bode plots for the Au(MPA)-PPy/ITO-glass electrode and Ab-αCRP/Au(MPA)-PPy/ITO-glass bioelectrode are shown in Fig. 5b. The behavior of the two electrodes has been analyzed mainly in three regions of the frequency range. At the highest frequencies (>25 kHz) shown in Fig. 5b, where negligible changes in log Z value are observed for both the electrodes with respect to change in log f, the R_s circuit element dominates the impedance. In the low frequency region (<50 Hz) for Au(MPA)-PPy-modified electrode, a very small portion of the curve (f=28 to 151 Hz) showed R_{et} characteristics where impedance is almost independent of frequency. This R_{et} characteristic was replaced by the diffusive characteristic nature of the Au(MPA)-PPy film with increasing log Z value in the lower region of frequency (<28 Hz) due to the highly permeable and porous electrode surface structure. After the immobilization of protein, Ab-αCRP, the diffusive and porous behavior of the Au(MPA)-PPy film electrode changes to a charge transfer characteristic, R_{et}, in the low frequency range (<16 Hz). The presence of R_{et} characteristic in this low frequency range shows the biocompatible nature of the bioelectrode. In the intermediate frequency range (50 Hz to 25 kHz), an almost straight line with a slope of −1 with a high phase angle of ~40° was obtained in the case of a bioelectrode showing dominance of capacitive element CPE in this region for the bioelectrode, while the same phenomena with much smaller phase angle (~13°) has been observed for Au(MPA)-PPy-modified electrode in a smaller frequency range of 355 Hz to 25 kHz. This shows that in case of Au(MPA)-PPy-modified electrode, CPE remains dominant for a small frequency range only.

The heterogeneous electron transfer rate constant (k^0) values of the $[Fe(CN)_6]^{3-/4-}$ redox couple for the polymer modified electrode and, after protein immobilization, were determined by using R_{et} values obtained from their corresponding impedance plots. The k^0 values are calculated from the charge transfer kinetics represented by Eq. (3) and are given in Table 1:

$$k^0 = RT \Big/ n^2 F^2 A R_{et} C \tag{3}$$

where R is the gas constant, T is the temperature, n is the number of electrons involved in the electrode reaction, F is the Faraday constant, A is the area of the electrode, and C is the concentration of the redox couple in the bulk solution. A twofold increment in the k^0 value (Table 1) for Au(MPA)-PPy/ITO-glass electrode in comparison to native PPy/ITO-glass electrode shows that the rate of electron transfer at the nanocomposite electrode/solution interface is twice as fast than at the native PPy film-based electrode. A prominent decrease in k^0 of about one fourth after the immobilization of an insulating layer of protein Ab-αCRP on

Au(MPA)-PPy/ITO-glass electrode shows a sluggish electron charge transfer at the bioelectrode/solution interface.

The type of diffusion occurring at the spatially heterogeneous electrodes such as those represented by porous electrodes, partially blocked electrodes, microelectrode arrays, and electrodes made of composite materials can be estimated by employing a theoretical framework given by Davies and Compton [25, 26]. The diffusion layer thickness, δ, could be determined using the Einstein equation modified by the authors and represented by Eq. 4:

$$\delta = \left(2D\Delta E \Big/ \upsilon\right)^{1/2} \tag{4}$$

where D is the diffusion coefficient of aqueous ferrocyanide (6.3×10^{-6} cm^2 s^{-1}), ΔE is the potential width of the votammogram, and υ is the scan rate (0.05 V s^{-1}). The corresponding δ values of ~56 μm obtained for different modified electrodes show a case 3 type of behavior of the voltammetric responses at spatially heterogeneous electrodes which is associated with an overlap of adjacent diffusion layers resulting from the small size of the inert part of the electrode [27].

Electrochemical Impedance Response to Antigen

Electrochemical impedance response of the bioelectrode toward the detection of protein antigen, Ag-αCRP, was carried out in 0.1 M KCl solution containing 2 mM $[Fe(CN)_6]^{3-}$/$[Fe(CN)_6]^{4-}$ (pH 7.4, 1.5 mL), at the scanning frequency range from 0.1 Hz to 100 kHz. The rationale behind selecting the said frequency range of impedance spectra is that at very low frequencies (f<0.1 Hz), the impedance value is basically determined by the DC conductivity of the electrolyte solution, while at very high frequencies (f>100 kHz), inductance of the electrochemical cell and connecting wires could contribute to the impedance spectra. Thus, to obtain the analytically meaningful impedance spectra, the frequency range of 0.1 Hz<f< 100 kHz has been selected where they are mainly controlled by the interfacial properties of the modified electrodes. The R_{et} value of the bioelectrode corresponding to a sample solution containing no protein antigen was taken as the control sample response. The corresponding Nyquist plots of the bioelectrode for different concentrations of the antigen Ag-αCRP solution are shown in Fig. 6a. It was found that the R_{et} value increases (Table 2) considerably with a change in the diameter of the semicircle portion of the Nyquist plot after successive addition of aliquots of different concentrations of the protein antigen, Ag-αCRP. This can be explained on the basis of perturbation causing the interfacial electron transfer along the bioelectrode/solution interface, resulting from the kinetic barrier generated by the antibody-antigen immunoreaction on the bioelectrode surface. As the Faradaic reaction of a redox couple becomes increasingly hindered, the R_{et} value increases and the Y_0 value decreases accordingly (Table 2). The value of k^0 simultaneously decreases with increasing immunoreaction indicating the formation of an insulating protein complex layer on the bioelectrode which retards the rate of the electron transfer reaction.

The impedance modulus Bode plot of the bioelectrode (Fig. 6b) is helpful in explaining the role of different circuit elements in different frequency regions and consequently helpful in explaining various kinetic phenomena occurring at the bioelectrode surface during immunoreaction. The high frequency region, i.e., above 1 kHz, corresponds to solution resistance element R_s which remains unchanged with respect to frequency, while in the low frequency region (<10 Hz), R_{et} and Z_w remain dominant. The mid-frequency region from 10 Hz to 1 kHz shows a straight line with a

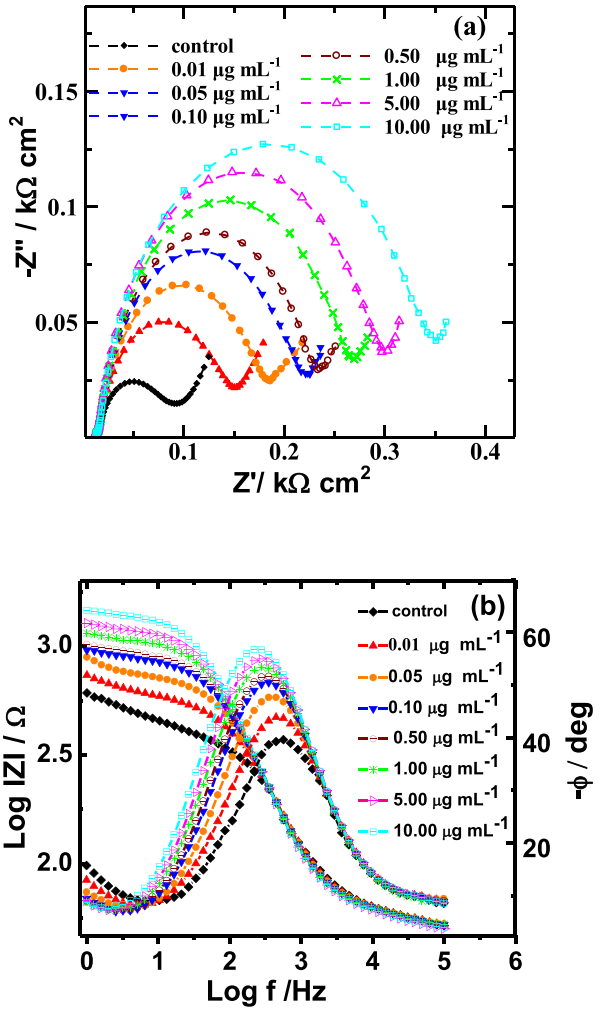

Fig. 6 **a** Faradaic impedance spectra of the bioelectrode before and after incubating with different concentrations of Ag-αCRP in PBS (pH 7.4) with 0.1 M KCl solution containing 2 mM $[Fe(CN)_6]^{3-/4-}$. **b** Corresponding Bode plots

maximum phase angle corresponding to the circuit capacitive element, CPE. It is to be noted that with increasing immunoreaction, in the very low frequency region, there is a consistent decrease in the phase angle, suggesting the increase in R_{et} behavior at low frequency region with immunoreaction. This also validates our choice of selecting the change in R_{et} value as the main sensing element.

The sensitivity of the as-prepared bioelectrode was obtained by plotting a graph (Fig. 7) between the change in specific electron charge transfer resistance ($\Delta R_{et} = (R_{et})_{\text{after immunoreaction}} - (R_{et})_{\text{control}}$) and logarithmic value of target Ag-αCRP concentration in the range of 10 ng mL^{-1} to 10 μg mL^{-1}. Equation 5 depicts the linear relationship so obtained with slope of the line as the sensitivity of the bioelectrode:

Table 2 EIS characteristic parameters of the bioelectrode upon immunoreaction with different concentrations of Ag-αCRP

[Ag-αCRP]	R_{et} (Ω cm^2)	CPE		k^0 (m s^{-1})	Z_w (Ω cm^2)
		Y_0 (μF cm^{-2})	n		
Control	88.25	43.2	0.789	0.47×10^{-3}	2.01×10^{-3}
0.01 μg mL^{-1}	133.25	36.8	0.802	0.39×10^{-3}	2.23×10^{-3}
0.05 μg mL^{-1}	169.00	32.2	0.820	0.31×10^{-3}	2.43×10^{-3}
0.10 μg mL^{-1}	206.00	30.9	0.828	0.25×10^{-3}	3.09×10^{-3}
0.50 μg mL^{-1}	221.75	29.9	0.833	0.23×10^{-3}	3.25×10^{-3}
1.00 μg mL^{-1}	255.25	28.9	0.839	0.20×10^{-3}	3.23×10^{-3}
5.00 μg mL^{-1}	296.25	28.7	0.838	0.17×10^{-3}	3.34×10^{-3}
10.00 μg mL^{-1}	329.75	28.2	0.842	0.16×10^{-3}	3.43×10^{-3}

$$\Delta R_{et} = b\log[\text{Ag}{-}\alpha\text{CRP}] + d \tag{5}$$

The R_{et} sensitivity (slope b of the calibration curve) of the bioelectrode was found to be 46.27 Ω cm^2/decade of Ag-αCRP with an intercept d=114.43 Ω cm^2 having a correlation regression coefficient of 0.992 (n=7). The limit of detection was found to be 19.38 ng mL^{-1} based on three times of signal-to-noise ratio. A comparative analytical performance of some electrochemical-based systems for CRP detection is given in Table 3. The stability of the bioelectrode was also investigated by repeatedly carrying out the impedimetric response measurements for at least five times with the same concentration of Ag-αCRP, under identical experimental conditions. The obtained corresponding impedance response of the bioelectrode showed insignificant decay in the R_{et} value from its initial control value indicating the stability of the bioelectrode response in solution as well as in an open environment. The nonspecific adsorption is one of the major problems in immunosensing. The specificity of the bioelectrode toward the Ag-αCRP was investigated by exposing it to a nonspecific protein antigen, Ag-IgG, over the same concentration range of 10 ng mL^{-1} to 10 μg mL^{-1} under identical

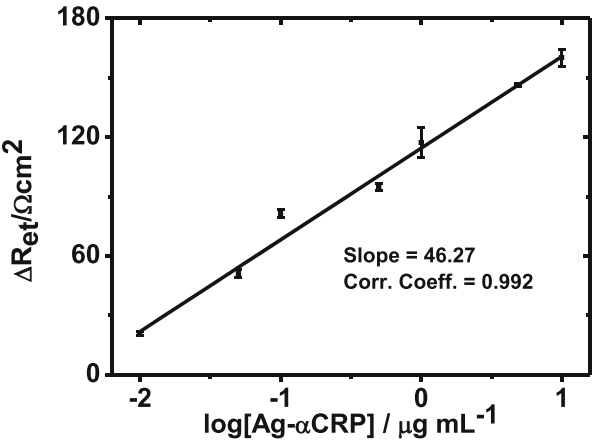

Fig. 7 Concentration-dependent calibration curve of bioelectrode; the *error bars* represent the standard deviation from three separate experiments

experimental conditions. The observation of a small change of ~5 to 8 % in response (ΔR_{et}) with respect to the control sample over the aforementioned concentration range of IgG indicated an insignificant contribution of a nonspecific interaction to the total bioelectrode response.

Conclusion

The site-specific covalent immobilization of Ab-αCRP to a one-step electrochemically synthesized Au(MPA)-PPy/ITO-glass electrode has been reported as an attractive platform for the quantitative analysis of human cardiac αCRP. The stepwise formation of the bioelectrode has been analyzed through different spectroscopic and electrochemical techniques. The nanocomposite film comprising of intercalated functionalized Au NPs provided a good biocompatible microenvironment for the immobilization of Ab-αCRP biomolecules with retention of the biological activity and also promoted the stability of the bioelectrode. The dominance of R_{et} behavior in the low frequency region of the EIS spectra of the bioelectrode exhibited a biocompatible nature. High protein loading with efficient covalent bonding to the Au(MPA) results in the construction of a bioelectrode showing a wider linear detection range with good sensitivity, biocompatibility, and acceptable reproducibility. The technique used to immobilize the antibody on the electrode surface and the methodology employed to analyze the bioelectrode response is sufficiently general, reliable, and sensitive to detect increases in the R_{et} upon antigen binding at concentrations relevant for the early stage detection of acute myocardial infarction (AMI) which is the leading cause of morbidity and mortality worldwide. The bioelectrode exhibited a linear impedance response to CRP in the range of 10 ng to 10 μg mL^{-1} in phosphate buffer (pH 7.4) at the low frequency region of <10 Hz with a R_{et} sensitivity of 46.27Ω cm^2/decade of [Ag-αCRP].

Acknowledgments We are grateful to Prof. R. C. Budhani, Director, National Physical Laboratory, New Delhi, India for providing the facilities. S.K. Mishra is thankful to the Council of Scientific and Industrial Research, India for providing a senior research fellowship (SRF). We also acknowledge Mr. Sandeep Singh for AFM measurements.

Table 3 Comparison of analytical performance of electrochemical sensors for Ag-αCRP

Electrochemical sensor type	Transduction platform	Linear range (ng mL^{-1})	Limit of detection (LOD) (ng mL^{-1})	References
EIS	SAM/Au electrode	60 to 6,000	19	[28]
EIS	Ab-BSA/Au NPs/Cyst/Au electrode	5,000 to 25,000	–	[29]
Capacitance	Interdigitated Au electrodes on nanocrystalline diamond surface	25 to 800	–	[30]
Square-wave anodic stripping voltammetry	Poly(dimethylsiloxane)-Au nanoparticle	0.5 to 200	~0.24	[31]
EIS	NHS/MUA/MPA/Au electrode	45 to 5,840	30	[32]
EIS	Au(MPA)-PPy/ITO-glass	10 to 10,000	19.38	Present work

References

1. Ates, M. (2013). *Materials Science and Engineering: C, 33*, 1853–1859.
2. Yuan, L., Wei, W., & Liu, S. (2012). *Biosensors and Bioelectronics, 38*, 79–85.
3. Revin, S. B., & John, S. A. (2012). *Analyst, 137*, 209–215.
4. Park, S. J., Kwon, O. S., & Jan, J. (2013). *Chemical Communications, 49*, 4673–4675.
5. Singh, M., Kathuroju, P. K., & Jampana, N. (2009). *Sensors and Actuators, B, 143*, 430–443.
6. Jia, Y., Xiao, P., He, H., Yao, J., Liu, F., Wang, Z., et al. (2012). *Applied Surface Science, 258*, 6627–6631.
7. Dong, Z. H., Wei, Y. L., Shi, W., & Zhang, G. A. (2011). *Materials Chemistry and Physics, 131*, 529–534.
8. Shi, W., & Ma, Z. (2011). *Biosensors and Bioelectronics, 26*, 3068–3071.
9. Cao, X., Ye, Y., & Liu, S. (2011). *Analytical Biochemistry, 417*, 1–16.
10. Rajesh, Sharma, V., Mishra, S. K., & Biradar, A. M. (2012). *Materials Chemistry and Physics, 132*, 22–28.
11. Qiu, L., Peng, Y., Liu, B., Lin, B., Peng, Y., Malik, M. J., et al. (2012). *Applied Catalysis A, 413*, 230–237.
12. Ledue, T., & Rifai, N. (2003). *Clinical Chemistry, 49*, 1258–1271.
13. Kindt, T., Osborne, B., & Golsby, R. (2007). *Kuby immunology* (6th ed.). New York: W.H. Freeman.
14. Algarra, M., Gomes, D., & Esteves da Silva, J. C. G. (2012). *Clinica Chimica Acta, 415*, 1–9.
15. McDonnell, B., Hearty, S., Leonard, P., & O′ Kennedy, R. (2009). *Clinical Biochemistry, 42*, 549–561.
16. Lin, K. C., Kunduru, V., Bothara, M., Rege, K., Prasad, S., & Ramakrishna, B. L. (2010). *Biosensors and Bioelectronics, 25*, 2336–2342.
17. Yang, T., Wang, S., Jin, H., Bao, W., Huang, S., & Wang, J. (2013). *Sensors and Actuators, B, 178*, 310–315.
18. Suprun, E. V., Shilovskaya, A. L., Lisitsa, A. V., Bulko, T. V., Shumyantseva, V. V., & Archakov, A. I. (2011). *Electroanalysis, 23*, 1051–1057.
19. Xu, H., Wang, L., Ye, H., Yu, L., Zhu, X., Lin, Z., et al. (2012). *Chemical Communications, 48*, 6390–6392.
20. Guo, X., Kulkarni, A., Doepke, A., Halsall, B. H., Iyer, S., & Heineman, W. R. (2012). *Analytical Chemistry, 84*, 241–246.
21. Wei, Q., Zhao, Y., Du, B., Wu, D., Li, H., & Yang, M. (2012). *Food Chemistry, 134*, 1601–1606.
22. Shi, Y., Wang, H., & Cai, N. (2012). *Journal of Power Sources, 208*, 24–34.
23. Sen, T., & Patra, A. (2009). *Journal of Physical Chemistry C, 113*, 13125–13132.
24. Shamsipur, M., Asgari, M., Maragheh, M. G., & Moosavi-Movahedi, A. A. (2012). *Bioelectrochemistry, 83*, 31–37.
25. Davies, T. J., Banks, C. E., & Compton, R. G. (2005). *Journal of Solid State Electrochemistry, 9*, 797–808.
26. Compton, R. G., & Banks, C. E. (2007). *Understanding voltammetry*. London: World Scientific.
27. Solomon, A., Mamuru, Kenneth, I., & Ozoemena, I. (2010). *Electroanalysis, 22*, 985–994.
28. Bryan, T., Luo, X., Bueno, P. R., & Davis, J. J. (2013). *Biosensors and Bioelectronics, 39*, 94–98.
29. Zhu, Jie, J., Xu, Zhong, J., He, Tao, J., et al. (2003). *Analytical Letters, 36*, 1547–1556.
30. Quershi, A., Gurbuz, Y., Kang, W. P., & Davidson, J. L. (2009). *Biosensors and Bioelectronics, 25*, 877–882.
31. Zhou, F., Lu, M., Wang, W., Bian, Z. P., Zhang, J. R., & Zhu, J. J. (2010). *Clinical Chemistry, 56*, 1701–1707.
32. Puri, N., Tanwar, V. K., Sharma, V., Ahuja, T., Biradar, A. M., & Rajesh. (2010). *International Journal of Integrative Biology, 9*, 1–5.